

# Source Shot Noise Mitigation in Focused Ion Beam Microscopy by Time-Resolved Measurement

Minxu Peng<sup>a</sup>, John Murray-Bruce<sup>a</sup>, Karl K. Berggren<sup>b</sup>, Vivek K Goyal<sup>a,\*</sup>

<sup>a</sup>Department of Electrical and Computer Engineering, Boston University, Boston, MA, 02215, US

<sup>b</sup>Department of Electrical Engineering and Computer Science, Massachusetts Institute of Technology, Cambridge, MA 02139, US

## Abstract

Focused ion beam (FIB) microscopy suffers from source shot noise – random variation in the number of incident ions in any fixed dwell time – along with random variation in the number of detected secondary electrons per incident ion. This multiplicity of sources of randomness increases the variance of the measurements and thus worsens the trade-off between incident ion dose and image accuracy. Time-resolved sensing combined with maximum likelihood estimation from the resulting sets of measurements greatly reduces the effect of source shot noise. Through Fisher information analysis and Monte Carlo simulations, the reduction in mean-squared error or reduction in required dose is shown to be by a factor approximately equal to the secondary electron yield. Experiments with a helium ion microscope (HIM) are consistent with the analyses and suggest accuracy improvement for a fixed source dose, or reduced source dose for a desired imaging accuracy, by a factor of about 3.

**Keywords:** compound Poisson distributions, electron microscopy, Fisher information, helium ion microscopy, Neyman Type A distribution, source shot noise

## 1. Introduction

State-of-the-art techniques for imaging the structure of a sample at near-atomic resolution depend on the use of microscopes that scan the sample with a focused beam of particles. For instance, a focused electron beam is employed in scanning electron microscopy (SEM) [1], laser beams in confocal laser-scanning microscopy [2] and two-photon laser-scanning fluorescence microscopy [3], and helium ion beams in helium ion microscopy (HIM) [4]. A fundamental goal with these technologies is to aim to produce the best image quality for a given number of incident particles. This is especially relevant when each incident particle appreciably damages the sample; thus, we henceforth concentrate on HIM.

Focused ion beam (FIB) imaging methods have randomness in the number of incident particles (the *source shot noise*) and in the influence of each incident particle on the instrument measurement. The goal of the imaging is to infer properties of the sample that are revealed through the number of detected secondary electrons (SEs) per incident ion, and the source shot noise is detrimental to this effort because it is unrelated to the sample. Presumably, we would prefer to have a precisely known number of incident ions.

The main idea of this work is that time-resolved measurement of SEs can be used to mitigate the effect of source shot noise. In certain limiting cases, we can completely eliminate the effect of source shot noise, producing estimation performance equivalent to a deterministic incident ion beam. More

importantly, for parameters that reasonably model HIM, the improvement is substantial and validated by both simulations and experiments.

The key technical result is an analysis of Fisher information gain and the consequent observation that information gain per incident particle is maximized when the number of incident particles per measurement trial is low (e.g., from a combination of low dwell time and low beam current). Based on this, we advocate for combining information from multiple low-intensity acquisitions, which we term *time-resolved* (TR) measurement. We first presented the TR measurement concept for FIB microscopy in [5].

### 1.1. Background

The first image of a solid sample based on secondary electrons emitted in response to an electron beam scanner was produced by Knoll in 1935, inspiring the development of a dedicated SEM [1]. Ever since their development, SEMs have been ubiquitous in both research and industrial imaging, as well as in nanometerological applications [6]. Building upon decades of research in focused ion beam microscopy, the first commercial HIM was introduced in 2006 [4, 7], with the promise of producing images with sub-nanometer resolution [8] and reduced charging of the sample, when compared with SEM. However just like SEM, HIM uses a focused particle beam to produce lateral spatial resolution in a ballistic configuration [4]. Both material composition (e.g., atomic number) and shape (topographic yield variations common to SEM as well) contribute to the number of SEs dislodged from the specimen [9]. These properties, along with improved diffraction-limited imaging resolution and reduced sample charging, have enabled superior

\*Corresponding author.

Email address: v.goyal@ieee.org (Vivek K Goyal)

imaging of insulators without the need for metal coating. Hence HIM is an important imaging technology for semiconductor and nanofabrication research [10].

Notwithstanding the progress in the pursuit of ultra-high resolution, these imaging technologies all have the disadvantage of causing damage to the sample through sputtering [11, 12, 13]. Whilst sample damage can have especially severe impact on biological samples, it also occurs for many other types of materials. It is thus recognized and modeled as a fundamental limit to imaging with focused beams. With the helium ion being 7300 times more massive than the electron, mitigating sample damage in HIM is paramount. One possible approach is imaging using lower ion doses but at the cost of image lower quality [12]. Consequently, studies analyzing the extent of beam damage and establishing safe imaging dose have appeared [14, 15].

### 1.2. Main contributions

- Introduction of time-resolved measurement as a mechanism for mitigation of source shot noise in FIB microscopy.
- Introduction of mathematical models for FIB microscopy with a Poisson number of incident ions, Poisson number of SEs per incident ion, and direct or indirect detection of the SEs.
- Quantitative analyses of Fisher information gain for the above models, including comprehensible expressions for the low- and high-dose limits for the direct-detection model.
- Experimental demonstration of the use of time-resolved measurement using data from a Zeiss ORION NanoFab HIM. Despite a lack of ground truth, evidence of improvements over conventional image formation is compelling.

### 1.3. Outline

In Section 2, we present our baseline measurement model and basic analyses of this model. These analyses provide the foundations for our development, in Section 3, of the advantage provided by dividing any fixed ion dose into small doses through time-resolved measurement. We present both abstract numerical results and image simulations. Inspired by the indirect detection of SEs in current HIM instruments, Section 4 introduces suitable models and studies the theoretical improvement factors from time-resolved measurement. Section 5 presents experimental results using data from a Zeiss HIM.

## 2. Single measurement: model and analyses

Two main components enable FIB imaging: a stable source to generate the FIB and a detector to measure the number of SEs leaving the sample's surface. Due to ion-sample interaction, SEs become excited and dislodged from the sample's surface [16], accelerating towards the SE detector. Imaging is achieved by raster scanning the ion beam with some fixed dwell

time per pixel. For each pixel, detected SEs are mapped to a grayscale level, hence producing an image of the sample.

During the acquisition process, for any fixed dwell time there is randomness in the number of ions reaching the sample. In addition, for each ion that interacts with the sample, there is randomness in the number of emitted SEs. In this section, we discuss a ‘‘Poisson–Poisson’’ model in which both the numbers of ions and the numbers of SEs induced by each ion follow Poisson distributions. With this model, the estimability of mean SE yield is amenable to theoretical analysis through Fisher information. The analyses of this section are used to support the use of time-resolved measurement in Section 3, and richer models are considered in Section 4. All the analyses and methods of this paper are applied separately for each micrograph pixel, so we do not include any pixel indexing.

### 2.1. A Poisson–Poisson model for FIB imaging

In our abstraction, an ion beam incident on the sample for a fixed dwell time  $t$  has ion arrivals following a Poisson process with rate  $\Lambda$  per unit time. Hence, the number of incident ions  $M$  is a Poisson random variable with mean  $\lambda = \Lambda t$ . Ion  $i$  produces a number of SEs  $X_i$  following a Poisson distribution with mean  $\eta$ . Since emitted SEs travel a very short distance before being captured by the SE detector, we model the SE detections as instantaneous and simultaneous. The fundamental assumption is that the delay before SE detection is much less than a typical ion interarrival time; this places some upper limit on the ion beam currents at which our model is reasonable.

The goal is to produce an estimate of  $\eta$  from the total detected SEs

$$Y = \sum_{i=1}^M X_i, \quad (1)$$

with  $\lambda$  known. Notice that  $Y$  is a sum of  $M$  independent Poisson random variables where the unknown  $M$  is itself also a Poisson random variable. As shown in Appendix A,  $Y$  is an example of a compound Poisson random variable; specifically, it has the so-called *Neyman Type A* distribution [17, 18], with probability mass function (PMF)

$$P_Y(y; \eta, \lambda) = \frac{e^{-\lambda} \eta^y}{y!} \sum_{m=0}^{\infty} \frac{(\lambda e^{-\eta})^m m^y}{m!}, \quad (2)$$

mean

$$E[Y] = \lambda \eta, \quad (3)$$

and variance

$$\text{var}(Y) = \lambda \eta + \lambda \eta^2. \quad (4)$$

Ward et al. [19] demonstrated empirically that this is an accurate model for numbers of detected SEs in an experimental setup involving a gallium ion beam.

### 2.2. Baseline estimator

It follows from (3) that simple scaling,

$$\hat{\eta}_{\text{baseline}}(Y) = \frac{Y}{\lambda}, \quad (5)$$

gives an unbiased estimate of  $\eta$ . The mean-squared error (MSE) of this estimate,

$$\begin{aligned} \text{MSE}(\hat{\eta}_{\text{baseline}}) &= \mathbb{E}[(\eta - \hat{\eta}_{\text{baseline}}(Y))^2] \\ &= \frac{\text{var}(Y)}{\lambda^2} = \frac{\eta(1 + \eta)}{\lambda}, \end{aligned} \quad (6)$$

thus follows from (4). In imaging (in contrast to metrology), the scaling may be arbitrary; thus, when every pixel has the same mean dose  $\lambda$ , the SE counts can be used directly to form a reasonable image.

Assuming for the moment that  $\lambda$  is an integer, if the number of incident ions were deterministically  $\lambda$ , the baseline estimator would be the sample mean of  $\{X_i\}_{i=1}^\lambda$ . Furthermore, it would be the maximum likelihood (ML) estimator of  $\eta$ , it would again be unbiased, and its MSE would be  $\eta/\lambda$ . The factor of  $(1 + \eta)$  excess seen in (6) is the cost of the randomness of a Poisson ion beam. We will see approximately this factor of improvement from time-resolved measurement, thus approximately cancelling the effect of source shot noise.

### 2.3. Oracle estimator

If one were able to know  $M$ , the estimate

$$\hat{\eta}_{\text{oracle}}(Y, M) = \frac{Y}{M} \quad (7)$$

would be superior to  $\hat{\eta}_{\text{baseline}}$  because  $Y$  is the sum of  $M$  random variables, each with mean  $\eta$ . One can view  $\hat{\eta}_{\text{oracle}}$  as mitigating the source shot noise by using the exact number of ions. Along with the issue of resolving 0/0 when no ions are incident, the problem with this is that  $M$  is not observable. While the exact number of ions  $M$  cannot be known exactly from only observing  $Y$ , we will see that  $M$  becomes approximately known with time-resolved measurement.

For a non-Bayesian analysis of  $\hat{\eta}_{\text{oracle}}$ , we can fix an arbitrary value  $\eta_0$  as the estimate produced when  $M = 0$ . While  $\hat{\eta}_{\text{oracle}}$  is unbiased whenever  $M > 0$  (which can be seen by iterated expectation with conditioning on  $M$ ), there is nothing computable from the data  $(Y, M) = (0, 0)$  that makes  $\hat{\eta}_{\text{oracle}}$  unbiased overall. Specifically,

$$\begin{aligned} \text{bias}(\hat{\eta}_{\text{oracle}}) &= \mathbb{E}[\hat{\eta}_{\text{oracle}}(Y, M)] - \eta \\ &\stackrel{(a)}{=} \mathbb{E}[\mathbb{E}[\hat{\eta}_{\text{oracle}}(Y, M) | M]] - \eta \\ &\stackrel{(b)}{=} \eta_0 \mathbb{P}(M = 0) + \eta(1 - \mathbb{P}(M = 0)) - \eta \\ &\stackrel{(c)}{=} \eta_0 e^{-\lambda} + \eta(1 - e^{-\lambda}) - \eta \\ &= (\eta_0 - \eta)e^{-\lambda}, \end{aligned} \quad (8)$$

where (a) follows from the law of iterated expectation; (b) from  $\mathbb{E}[\hat{\eta}_{\text{oracle}}(Y, M) | M = m]$  taking only the values  $\eta_0$  and  $\eta$ ; and (c) from the Poisson distribution of  $M$ . The variance of the estimate is

$$\begin{aligned} \text{var}(\hat{\eta}_{\text{oracle}}) &\stackrel{(a)}{=} \mathbb{E}[\text{var}(\hat{\eta}_{\text{oracle}}(Y, M) | M)] + \text{var}(\mathbb{E}[\hat{\eta}_{\text{oracle}}(Y, M) | M]) \\ &\stackrel{(b)}{=} \eta \sum_{m=1}^{\infty} \frac{1}{m} e^{-\lambda} \frac{\lambda^m}{m!} + e^{-\lambda}(1 - e^{-\lambda})(\eta - \eta_0)^2 \\ &\stackrel{(c)}{=} \eta g(\lambda) + e^{-\lambda}(1 - e^{-\lambda})(\eta - \eta_0)^2, \end{aligned} \quad (9)$$

where (a) follows from the law of total variance; (b) from the conditional distribution of  $\hat{\eta}_{\text{oracle}}$  being the constant  $\eta_0$  for  $M = 0$  and the sample mean of  $m$  Poisson( $\eta$ ) random variables for  $M = m$ ,  $m > 0$ ; and (c) introduces a function  $g(\lambda) = \sum_{m=1}^{\infty} (1/m) e^{-\lambda} \lambda^m / m!$ , which has no elementary closed form. Notice that  $g(\lambda) \approx \lambda$  for  $\lambda \ll 1$ , since only the  $m = 1$  term is appreciable; moreover, it can be shown that  $g(\lambda) \approx 1/\lambda$  for  $\lambda \gg 1$ .

The bias and variance computations can be combined to give an expression for the MSE of the oracle estimator:

$$\begin{aligned} \text{MSE}(\hat{\eta}_{\text{oracle}}) &= [\text{bias}(\hat{\eta}_{\text{oracle}})]^2 + \text{var}(\hat{\eta}_{\text{oracle}}) \\ &\stackrel{(a)}{=} [(\eta_0 - \eta)e^{-\lambda}]^2 + \eta g(\lambda) + e^{-\lambda}(1 - e^{-\lambda})(\eta - \eta_0)^2 \\ &= \eta g(\lambda) + e^{-\lambda}(\eta - \eta_0)^2, \end{aligned} \quad (10)$$

where (a) follows by substituting (8) and (9). Furthermore,

$$\text{MSE}(\hat{\eta}_{\text{oracle}}) \geq \eta g(\lambda), \quad (11)$$

with the bound achieved when  $\eta_0 = \eta$ . We stress that this bound is unachievable because  $\eta$  is not *a priori* known.

### 2.4. Fisher information

The MSE of any unbiased estimator is lower bounded by the reciprocal of the Fisher information via the Cramér–Rao bound (CRB) [20]. Fisher information is also central to our explanation of why time-resolved measurement combined with ML estimation greatly mitigates source shot noise.

The Fisher information for the estimation of  $\eta$  from  $Y$  in the Poisson–Poisson model, with  $\lambda$  a known parameter, can be simplified to

$$\begin{aligned} \mathcal{I}_Y(\eta; \lambda) &= \mathbb{E} \left[ \left( \frac{\partial \log P_Y(Y; \eta, \lambda)}{\partial \eta} \right)^2 ; \eta \right] \\ &= \sum_{y=0}^{\infty} \left( \frac{y}{\eta} - \frac{P_Y(y+1; \eta, \lambda)}{P_Y(y; \eta, \lambda)} \frac{y+1}{\eta} \right)^2 P_Y(y; \eta, \lambda); \end{aligned} \quad (12)$$

see Appendix B for a derivation. While this expression is not readily comprehensible, it can be used to compute  $\mathcal{I}_Y(\eta; \lambda)$  numerically and to derive certain useful asymptotic approximations and limits.

One can study  $\mathcal{I}_Y(\eta; \lambda)/\lambda$  as the information gain per incident ion. As illustrated in Figure 1, this *normalized Fisher information* (NFI) is a decreasing function of  $\lambda$ , with

$$\lim_{\lambda \rightarrow 0} \frac{\mathcal{I}_Y(\eta; \lambda)}{\lambda} = \frac{1}{\eta} - e^{-\eta} \quad (13)$$

and

$$\lim_{\lambda \rightarrow \infty} \frac{\mathcal{I}_Y(\eta; \lambda)}{\lambda} = \frac{1}{\eta(1 + \eta)} = \frac{1}{\eta} - \frac{1}{1 + \eta}, \quad (14)$$

as derived in Appendix C. The ratio of these limits is

$$\beta(\eta) = (1 + \eta)(1 - \eta e^{-\eta}), \quad (15)$$

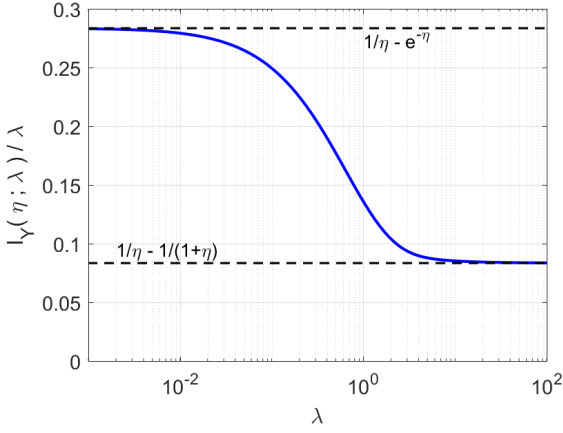


Figure 1: Normalized Fisher information  $\mathcal{I}_Y(\eta; \lambda)/\lambda$  as a function of  $\lambda$  for  $\eta = 3$ . Low-dose measurements are more informative per incident ion than high-dose measurements. The marked asymptotes are derived in [Appendix C](#).

which varies from 1 to  $\approx 1 + \eta$  as  $\eta$  increases from 0. Recall the  $1 + \eta$  factor arose in [Section 2.2](#) as the cost of randomness of a Poisson ion beam.

Comparing (14) with (6), we see that, asymptotically for large  $\lambda$ , the baseline estimator achieves the CRB. In contrast, for low  $\lambda$ , the probability for  $M = 0$  is appreciable, so there is no (even approximately) unbiased estimator.

### 3. Time-resolved measurements

Taken together, the analyses in [Section 2](#) suggest that there may be a way for the baseline estimate from (5) to be improved upon to give a reduction in MSE by the factor in (15). Time-resolved measurement indeed achieves this improvement. We examine this first through Fisher information and then through simulated performance of the ML estimator for imaging.

#### 3.1. Fisher information ratios

If we divide pixel dwell time  $t$  into  $n$  sub-acquisitions to obtain  $Y_1, Y_2, \dots, Y_n$ , these are independent and obtained with  $\lambda$  replaced by  $\lambda/n$ . The FI for the set of sub-acquisitions together is

$$\mathcal{I}_Y^{\text{TR}}(\eta; \lambda, n) \stackrel{(a)}{=} n \mathcal{I}_Y(\eta; \lambda/n) \quad (16)$$

$$\begin{aligned} &= \lambda \frac{\mathcal{I}_Y(\eta; \lambda/n)}{\lambda/n} \\ &\stackrel{(b)}{\approx} \lambda \left( \frac{1}{\eta} - e^{-\eta} \right), \end{aligned} \quad (17)$$

where (a) follows from the additivity of FI over independent observations; and (b) holds for large enough  $n$  because of (13). Without time-resolved measurement, for total dose values useful for imaging (say,  $\lambda > 2$ ), as illustrated in [Figure 1](#), the limit in (14) provides a good approximation of the FI:

$$\mathcal{I}_Y(\eta; \lambda) \approx \lambda \left( \frac{1}{\eta} - \frac{1}{1 + \eta} \right). \quad (18)$$

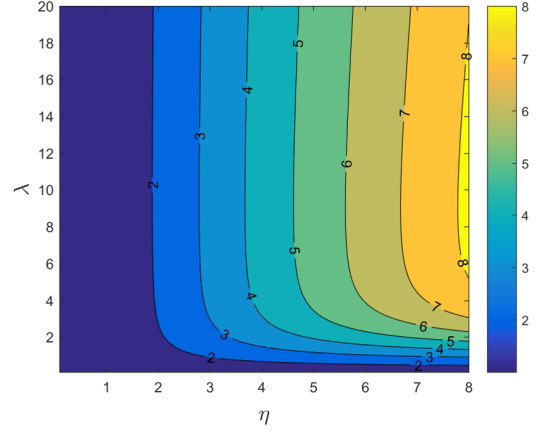


Figure 2: Fisher information ratio for Poisson–Poisson model used to predict the multiplicative factor by which MSE would be improved with the introduction of time-resolved measurement into FIB microscopy ( $n = 500$ ).

The ratio of (17) and (18) was already computed as (15). This ratio gives a convenient way to evaluate the improvement from time-resolved measurement and data processing. [Figure 2](#) is a contour plot of the FI ratio (without using approximations) for  $n = 500$ . The ratio of Fisher informations is the reciprocal of the ratio of Cramér–Rao lower bounds. For example, where the contour is labeled 5, splitting the fixed dose  $\lambda$  into  $n = 500$  sub-acquisitions enables the reduction of the mean-squared errors (MSE) to 20% of the MSE value from a single full-dose experiment.

#### 3.2. Cramér–Rao bounds

The CRB informs us that no unbiased estimator can have variance lower than the reciprocal of the Fisher information. Thus, the FI for a single measurement (12) and for time-resolved measurement (16) imply bounds on MSE for unbiased estimators, as plotted in [Figure 3](#). The asymptotic approximation (17) implies a bound that applies to any unbiased estimator  $\hat{\eta}_{\text{TR}}$  computed from the time-resolved measurements:

$$\text{MSE}(\hat{\eta}_{\text{TR}}) \geq \frac{\eta/(1 - \eta e^{-\eta})}{\lambda}. \quad (19)$$

For the performance without time-resolved measurement, this should be contrasted with (6); the baseline estimator achieves the CRB asymptotically in large  $\lambda$ , and [Figure 1](#) illustrates that the asymptote is a good approximation for values of  $\lambda$  useful for imaging.

#### 3.3. Joint distribution and ML estimation

For time-resolved measurements, the joint distribution is

$$P_{Y_1, \dots, Y_n}(y_1, \dots, y_n; \eta, \lambda) = \prod_{k=1}^n P_Y(y_k; \eta, \lambda/n), \quad (20)$$

where  $P_Y(\cdot; \cdot, \cdot)$  is given by (2). Roughly speaking, when the sub-acquisitions are short enough (that is,  $n$  is large enough),



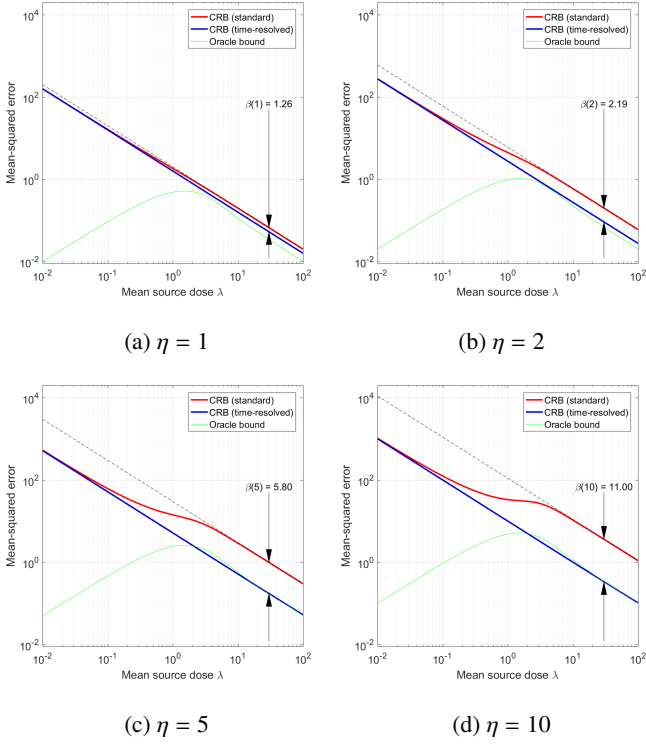


Figure 3: Comparison between the Cramér–Rao bounds obtained for conventional method (red, see (12)) and time-resolved measurement (blue,  $n = 10\,000$ , see (16)) for several values of mean secondary electron yield  $\eta$ . Also shown in each plot is the oracle bound (10) for the estimator (7); recall that this bound is based on estimator that is “increasingly unimplementable” as  $\lambda \rightarrow 0$  since it is derived from assuming  $\hat{\eta} = \eta$  when no ions are incident. Each plot also shows the performance from (6) for the baseline estimate, which is a high- $\lambda$  asymptote for the Cramér–Rao bound in the case of conventional sensing. The expression (19) is plotted as well, but it lies coincident with the blue curve.

each sub-acquisition will have very low dose and thus very likely have 0 or 1 incident ion. Assuming most sub-acquisitions with 1 incident ion yield at least 1 SE, one can use the number of sub-acquisitions with a strictly positive number of detected SEs as a proxy for the number of ions  $M$ . This gives some plausibility for mitigating source shot noise and is the intuitive justification of the “quotient mode” developed by Zeiss [21]. Our methods use the more precise model (20). Most importantly, we account for the probability of an incident ion resulting in zero detected SEs.

Given the observation  $(y_1, y_2, \dots, y_n)$ , the ML estimate for  $\eta$  is

$$\hat{\eta}_{\text{TR}} = \arg \max_{\eta} P_{Y_1, \dots, Y_n}(y_1, \dots, y_n; \eta, \lambda). \quad (21)$$

Since  $P_{Y_1, \dots, Y_n}(y_1, \dots, y_n; \eta, \lambda)$  is a non-convex function of  $\eta$ , we compute the optimization via grid search. This is not prohibitively complex because the decision variable is scalar.

### 3.4. Synthetic numerical results

Simulation results also demonstrate the improvement gained from time-resolved data acquisition and processing. For a fixed dose, a lower reconstruction MSE compared to the conventional method is obtainable; equivalently, time-resolved measurement

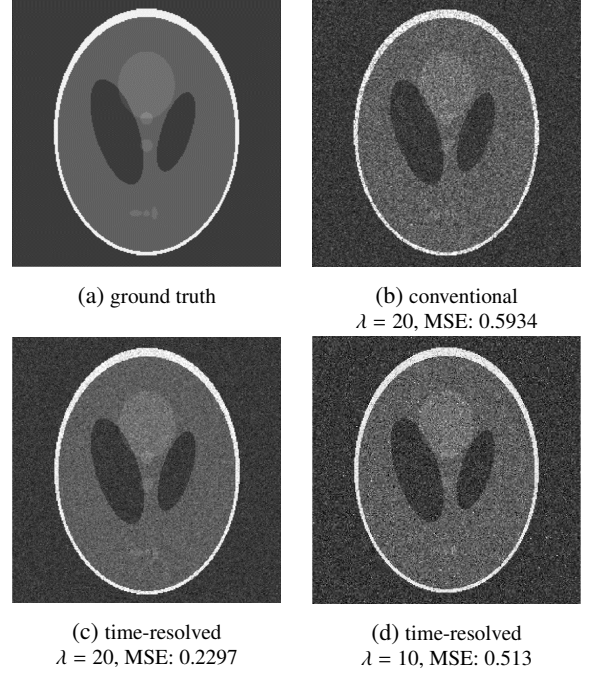


Figure 4: Simulated HIM experiment for a sample with mean secondary electron yield in  $[2, 8]$  for Poisson–Poisson (direct electron detection) model in Section 2.1. (a) Ground truth image. (b) Conventional HIM image with  $\lambda = 20$ . (c) and (d) Pixelwise ML estimates (21) computed from  $n = 100$  time-resolved measurements with  $\lambda = 20$  and  $\lambda = 10$ . Comparing (b) and (c) demonstrates MSE reduction at fixed dose. Comparing (b) and (d) demonstrates dose reduction without increase of MSE. These results do not use spatial regularization.

gives similar imaging MSE with a reduced ion dose compared to the conventional method.

Figure 4a shows the “Modified Shepp–Logan phantom” provided by the Matlab phantom command, at size  $256 \times 256$ , scaled to give ground truth SE values in the interval  $[2, 8]$ , as suggested in [22]. Figures 4b and 4c show that for a fixed dose of  $\lambda = 20$ , time-resolved measurement with  $n = 100$  sub-acquisitions achieves an MSE reduction by a factor of 2.4.

An alternative way to demonstrate the improvement due to time-resolved measurement is through a dose reduction for fixed image quality. The proposed time-resolved measurement reconstruction, shown in Figure 4d, achieves a slightly lower MSE than the conventional reconstruction in Figure 4b with a dose of only 10 ions per pixel.

## 4. Hierarchical compound models

The model introduced in Section 2.1 assumes direct secondary electron counting, so that the number of SEs is the final readout of the device. In current HIM instruments, the output is more indirect. We now discuss some plausible models for the SE detection process and show that FI-based analysis continues to suggest substantial advantages for time-resolved measurement.

### 4.1. Poisson–Poisson–Normal

In a typical HIM instrument, SEs emitted due to ion-sample interaction are accelerated towards a phosphor scintillator plate

by an electric field. Photons generated as a result of SE-scintillator interaction are amplified by a photomultiplier tube (PMT) and subsequently converted into an electrical current [23]. There is high degree of randomness in the scintillator and the PMT response [24], both of which cause randomness in the output current.

As one possible model with only two additional parameters, one could model the contribution to the final measurement from each detected SE as being normally distributed. Specifically, suppose the measured output current due to the  $j$ th SE is normal with mean  $c_1$  and variance  $c_2$ , i.e.,  $Z_j \sim \mathcal{N}(c_1, c_2)$ . Then, the observation model at one pixel becomes

$$U = \sum_{j=1}^Y Z_j, \quad (22)$$

where  $Y$  is the number of SEs. Combining the normal distribution with the Neyman Type A distribution in (2) gives the following probability density function (PDF) for  $U$ :

$$f_U(u; \eta, \lambda, c_1, c_2) = \sum_{y=1}^{\infty} \frac{1}{\sqrt{2\pi c_2 y}} \exp\left(-\frac{(u - c_1 y)^2}{2c_2 y}\right) P_Y(y; \eta, \lambda). \quad (23)$$

Under (23), the ML estimate of  $\eta$ , from  $n$  short acquisitions, becomes:

$$\hat{\eta}_{\text{TR}} = \arg \max_{\eta} f_{U_1, \dots, U_n}(u_1, \dots, u_n; \eta, \lambda, c_1, c_2), \quad (24)$$

where

$$f_{U_1, \dots, U_n}(u_1, \dots, u_n; \eta, \lambda, c_1, c_2) = \prod_{k=1}^n f_U(u_k; \eta, \lambda, c_1, c_2).$$

#### 4.2. Quantized Poisson–Poisson–Normal

While the Poisson–Poisson–Normal model of Section 4.1 attempts to account for randomness in the scintillator and PMT responses, several aspects of a typical HIM instrument are not modelled. In particular, (23) allows negative measurements and the analog-to-digital conversion (ADC) to map output current into an 8-bit gray scale value is unmodelled. Assuming analog gains are set to avoid ADC overload, both of these effects can be accounted for by rounding the measurement to its nearest non-negative integer. (Overload could be accounted for similarly.) Consequently, the PMF for the observed output  $\tilde{U} \in \mathbb{N}$  for each pixel is then:

$$P_{\tilde{U}}(\tilde{u}; \eta, \lambda, c_1, c_2) = \frac{\int_{\tilde{u}-\frac{1}{2}}^{\tilde{u}+\frac{1}{2}} f_U(u; \eta, \lambda, c_1, c_2) du}{\int_{-\frac{1}{2}}^{\infty} f_U(u; \eta, \lambda, c_1, c_2) du}. \quad (25)$$

Note that the denominator in (25) normalizes the PMF to account for there being no negative measurements. The corresponding ML estimate  $\hat{\eta}_{\text{TR}}$  under this new model can be written in a similar fashion to (24).

The FI for the estimation of  $\eta$  from  $\tilde{U}$ , with  $\lambda$ ,  $c_1$ , and  $c_2$  as known parameters, is

$$\mathcal{I}_{\tilde{U}}(\eta; \lambda, c_1, c_2) = \mathbb{E} \left[ \left( \frac{\partial \log P_{\tilde{U}}(\tilde{u}; \eta, \lambda, c_1, c_2)}{\partial \eta} \right)^2 ; \eta \right]. \quad (26)$$

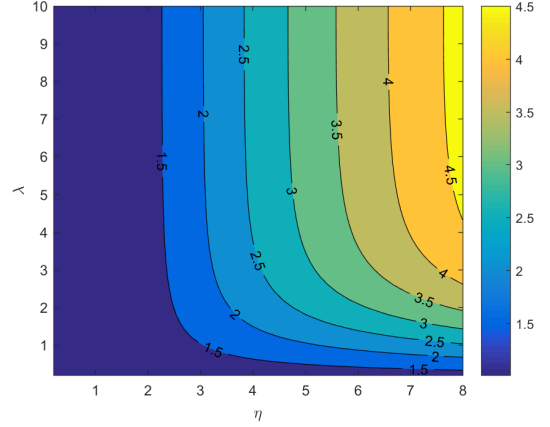


Figure 5: Fisher information ratio for Quantized Poisson–Poisson–Normal model used to predict the multiplicative factor by which MSE would be improved with the introduction of time-resolved measurement into FIB microscopy ( $c_1 = 10$ ,  $c_2 = 100$ , and  $n = 500$ ).

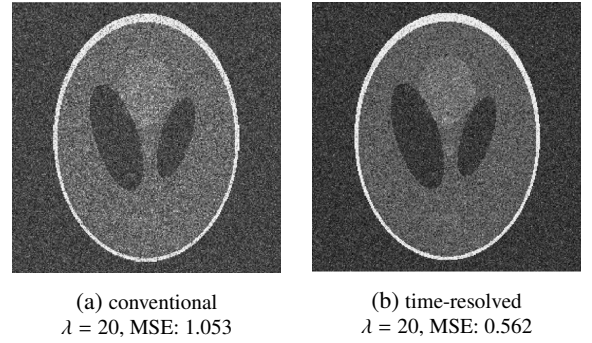


Figure 6: Simulated HIM experiment for Quantized Poisson–Poisson–Normal model in Section 4.2 when  $\lambda = 20$ ,  $c_1 = 10$ , and  $c_2 = 200$ : (a) Conventional HIM image. (b) Pixelwise ML estimates computed from  $n = 100$  time-resolved measurements. These results do not use spatial regularization.

Though we have no insightful simplifications or approximations of  $\mathcal{I}_{\tilde{U}}(\eta; \lambda, c_1, c_2)$ , we can compare it numerically to  $n \mathcal{I}_{\tilde{U}}(\eta; \lambda/n, c_1, c_2)$  to quantify the increase in information from TR measurements. A contour plot showing the Fisher information ratio for TR versus conventional data acquisition is given in Figure 5 under this new Quantized Poisson–Poisson–Normal hierarchical model. The plot suggests that improvement MSE improvements are still obtainable by using TR data. However, comparing it with Figure 2, it is clear that the overall possible gain is reduced in this new model. This is attributable to the extra layer of randomness introduced by the scintillator and PMT. In addition, this discrepancy can be viewed as theoretical support for preferring direct secondary electron counting, over other methods of electron detection.

Figure 6 shows the results of simulations for the same sample as in Figure 4. At the same dose of  $\lambda = 20$ , the MSEs are higher than in Figure 4, but substantial improvement from time-resolved measurement is again demonstrated.

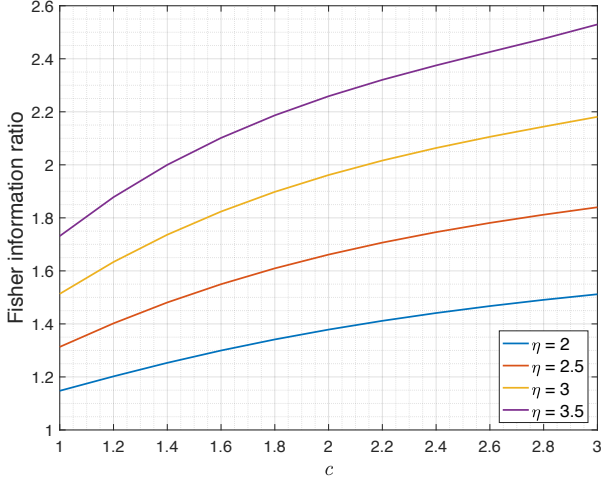


Figure 7: Fisher information ratio for Poisson–Poisson–Poisson model used to predict the multiplicative factor by which MSE would be improved with the introduction of time-resolved measurement into FIB microscopy (four values of  $\eta$ ,  $n = 500$ ,  $\lambda = 2$ ).

#### 4.3. Poisson–Poisson–Poisson

One final model further illustrates the flexibility of hierarchical modeling and the general potential of TR measurement. Removing the use of a normal distribution to model phosphor and PMT response, suppose that photons emitted by the scintillator can be directly measured instead of being converted into an electrical signal. Through the use of a time-resolved single-photon detector, we can count the number of emitted photons; for instance, a single photon avalanche diode (SPAD) detector with time-correlated single photon counting could be used. Modeling the number of photons generated due to the  $j$ th SE as a Poisson random variable  $W_j$  with mean  $c$  and the observation at one pixel by

$$V = \sum_{j=1}^Y W_j, \quad (27)$$

the PMF for the final read-out becomes

$$P_V(v; \eta, \lambda, c) = \sum_{y=0}^{\infty} \frac{e^{-cy}(cy)^v}{v!} \frac{e^{-\lambda}\eta^y}{y!} \sum_{m=0}^{\infty} \frac{(\lambda e^{-\eta})^m m^v}{m!}. \quad (28)$$

Equation (28) is obtained analogously to (23) by combining the Poisson distribution of  $W_j$  with the Neyman Type A distribution of  $Y$  given in (2).

Figure 7 shows plots of the Fisher information ratio for TR measurements under this Poisson–Poisson–Poisson model as a function of  $c$  for four  $\eta$  values when  $\lambda = 2$ . The plots show that improvements in MSE for a fixed dose (or dose reduction for a desired MSE) is expected when the proposed time-resolved sensing method is used.

## 5. HIM imaging results

### 5.1. Experiment details

Our methods were validated with data from a Zeiss ORION NanoFab HIM used to image a carbon-based defect on a sil-

icon substrate. The instrument was used to collect 128 sub-acquisitions of the sample using a 0.1 pA beam current and 200 ns dwell time, resulting in low ion dose of 0.125 ions per pixel. The image of one typical sub-acquisition is shown in Figure 8a. In this and all other panels of Figure 8, the scaling for display maps the range of the data linearly to the full black-to-white range.

With the set of 128 sub-acquisitions, we can emulate conventional and time-resolved image formation for doses from 0.125 ions per pixel to 16 ions per pixel. Conventional image formation has no time resolution; this is emulated by summing the sub-acquisitions, as shown in Figures 8c, 8d, and 8e. For our time-resolved method, since the instrument does not use direct electron detection and its output at each pixel is a nonnegative integer, the Quantized Poisson–Poisson–Normal model of Section 4.2 was employed. Hyper-parameters  $c_1 = 5$  and  $c_2 = 50$  were used without significant optimization. Results of pixel-by-pixel ML estimation under this model are shown in Figures 8h, 8i, and 8j. With increasing ion dose (moving from second to third to fourth column of Figure 8), the image quality improves as expected.

### 5.2. Quantitative evaluation

With no ground truth image of the sample available, any accuracy claims are delicate. We define the *MSE estimate*  $\widehat{\text{MSE}}$  for an image as the average of the squared difference between the image and a proxy for ground truth (Figure 8f) that is formed by taking the average of the two images produced using the conventional (Figure 8e) and time-resolved (Figure 8j) methods with all 128 sub-acquisitions. The difference is computed after scaling such that the mean brightness is matched to Figure 8f, on a 0 to 255 scale;<sup>1</sup> thus, the units of  $\widehat{\text{MSE}}$  are consistent but arbitrary. These MSE estimates appear in the captions of Figure 8. The choice of ground truth proxy is open to criticism, and more conservative quantitative comparisons are discussed in Section 5.3.

Comparing Figures 8b and 8g shows a reduction of  $\widehat{\text{MSE}}$  by a factor of 4.12 at very low dose, while comparing Figures 8c and 8h shows a reduction of  $\widehat{\text{MSE}}$  by a factor of 3.67. Similarly, comparing Figures 8d and 8i shows a reduction of  $\widehat{\text{MSE}}$  by a factor of 2.13. As discussed further in Section 5.3, the reduction in improvement factor in  $\widehat{\text{MSE}}$  as dose is increased is inevitable from the method of computing  $\widehat{\text{MSE}}$  and does not imply that improvement is diminishing.

An alternative is to assert a dose reduction. Comparing Figures 8d and 8h, the proposed time-resolved measurement method achieves slightly lower  $\widehat{\text{MSE}}$  with dose reduced by a factor of 3.

### 5.3. Conservative error analysis

While we believe  $\widehat{\text{MSE}}$  to be a reasonable metric, it is possible that it presents an inaccurate view of the improvement due to

<sup>1</sup>Some consideration of scaling is necessary because the TR method provides estimates of  $\eta$  (which usually is in [2, 8]), while the conventional estimate is a simple averaging of the output images of the HIM instrument, after data conversion and processing for display on a [0, 255] scale.



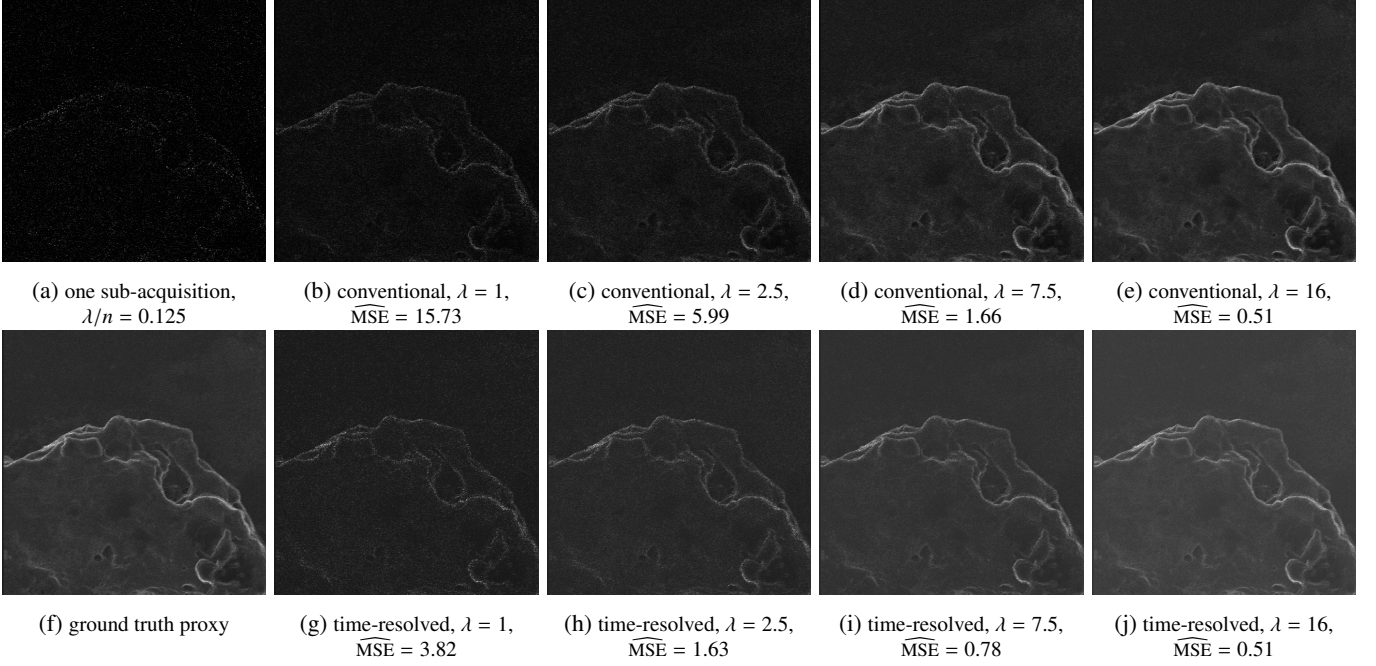


Figure 8: HIM experimental results for imaging a carbon-based defect on a silicon substrate sample. Results for our time-resolved method use the Quantized Poisson–Poisson–Normal compound model in Section 4.2 with  $c_1 = 5$  and  $c_2 = 50$ . All images are produced pixel-by-pixel (i.e., without spatial regularization). (a) A typical image from one sub-acquisition acquired with dose  $\lambda/n = 0.125$  ions per pixel. (b) Conventional method using 8 sub-acquisitions. (c) Conventional method using 20 sub-acquisitions. (d) Conventional method using 60 sub-acquisitions. (e) Conventional method using 128 sub-acquisitions. (f) Ground truth proxy with dose  $\lambda = 16$ , formed by averaging results shown in (e) and (j). (g) Time-resolved method using 8 sub-acquisitions. (h) Time-resolved method using 20 sub-acquisitions. (i) Time-resolved method using 60 sub-acquisitions. (j) Time-resolved method using 128 sub-acquisitions. Comparing (b) and (f) shows MSE reduction by a factor of 3.67 from our time-resolved method, and comparing (c) and (f) shows dose reduction by a factor of 3.0 without increase in MSE.

time-resolved sensing. Thus, we augment the comparison of  $\widehat{\text{MSE}}$  values with a decidedly more conservative approach.

Accumulating the sequence of 128 sub-acquisitions with conventional image formation creates a sequence of images, culminating in the  $\lambda = 16$  image shown in Figure 8e; similarly, the TR method creates a sequence culminating in Figure 8j. Treating Figure 8e as a ground truth proxy would be optimistic for the sequence of conventionally formed images and thus pessimistic for the sequence of images formed with the TR method. Conversely, treating Figure 8j as a ground truth proxy would be optimistic for the sequence of images formed with TR method and thus pessimistic for the sequence of conventionally formed images.<sup>2</sup> Using Figures 8e and 8j as ground truth proxies thus gives an optimistic MSE estimate  $\text{MSE}^-$  and pessimistic MSE estimate  $\text{MSE}^+$  for any image. These provide a range that is shown along with  $\widehat{\text{MSE}}$  in Figure 9.

While  $\text{MSE}^-$  and  $\text{MSE}^+$  are not rigorously lower and upper bounds to the MSE, they strengthen the evidence that the TR method provides a substantial improvement. For example, we see that for ion doses up to 4.5,  $\text{MSE}^+$  for the TR method is lower than  $\text{MSE}^-$  for the conventional method. Importantly, the convergences of curves for the conventional and TR methods at the

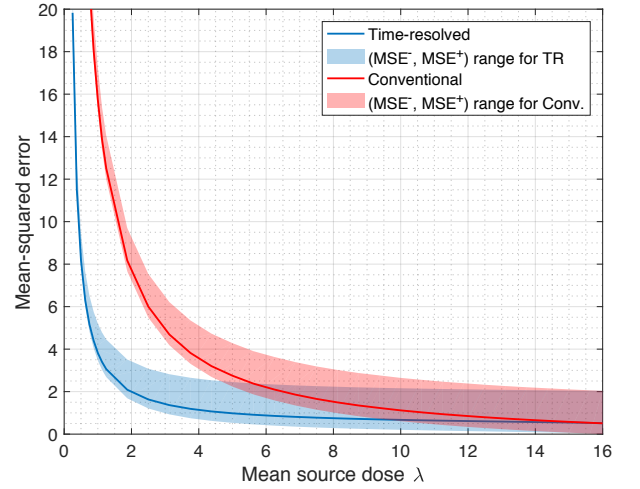


Figure 9: Estimated mean-squared error  $\widehat{\text{MSE}}$  (see Section 5.2) as a function of mean source dose  $\lambda$  for conventional (red) and time-resolved sensing (blue) methods. Also shown are the ranges  $(\text{MSE}^-, \text{MSE}^+)$  (see Section 5.3) intended to allow more conservative comparisons.

maximum ion dose of 16 should *not* be construed as showing diminishing advantage for the TR method at higher doses. As shown in Figure 9, the  $\text{MSE}^-$  values reach zero at whatever is the highest available ion dose, the  $\text{MSE}^+$  values reach the per-pixel Euclidean distance squared between Figures 8e and 8j, and the MSE values reach one quarter of that distance.

<sup>2</sup>Stated differently: Comparing a conventionally formed image to Figure 8e likely underestimates its error, while comparing it to Figure 8j likely overestimates its error. Conversely, comparing an image formed with the TR method to Figure 8j likely underestimates its error, while comparing it to Figure 8e likely overestimates its error.



## 6. Discussion

The main contribution of this paper is to introduce the idea that a set of low-dose focused ion beam microscope measurements can be substantially more informative than a single measurement with the same total dose. We refer to the acquisition of the set of low-dose measurements as “time-resolved measurement” because it can be realized by keeping beam current and total dwell time unchanged, while dividing the dwell time into short time segments.

Our demonstrations of the potential of TR measurements take a few forms. For a Poisson–Poisson model (Section 2.1) that serves as an abstract model for FIB measurement with direct detection of secondary electrons, we used normalized Fisher information to demonstrate that low-dose measurements are the most informative per incident ion (Figure 1) and yield a substantial multiplicative increase in FI (Figure 2); furthermore, we used simulations to demonstrate that ML estimation achieves performance improvement consistent with the FI increase (Figure 4). Indirect detection of secondary electrons can be modeled as well (Section 4). While analysis is made more complicated by these hierarchical models, FI computations and imaging simulations indicate that substantial improvements are still possible (Figures 5–7). Experiments with HIM data used a Quantized Poisson–Poisson–Normal model (Section 4.2) and demonstrated the advantage of TR measurements and processing, even without direct electron counting (Figures 8 and 9).

TR measurement is not a panacea, and this may become more intuitive by considering settings in which it provides no advantage. For example, keeping all else unchanged (aperture, electronic gain, etc.), when taking a digital photograph there is no advantage from dividing some appropriate exposure time into 100 shorter exposures. Since the original exposure time does not cause saturation, the 100 shorter-exposure photographs should simply be added together. If anything, the 100 shorter exposures is worse because each frame is subject to readout noise.

For a more formal demonstration, suppose i.i.d. Poisson random variables  $X_1, X_2, \dots, X_n$  are observed in analogy to time-resolved measurement, with observation of only  $X = \sum_{i=1}^n X_i$  as the counterpart *without* time resolution. If each  $X_i$  has mean parameter  $\lambda' = \lambda/n$ , then  $X$  is a Poisson random variable with mean parameter  $\lambda$ . There is no FI difference between  $(X_1, X_2, \dots, X_n)$  and  $X$  when the goal is estimation of  $\lambda$ , so time-resolved sensing does not provide any advantage in this case:

$$\begin{aligned} \mathcal{I}_{X_1, X_2, \dots, X_n}(\lambda) &= n \mathcal{I}_{X_1}(\lambda) \stackrel{(a)}{=} n \frac{1}{n^2} \mathcal{I}_{X_1}(\lambda') \stackrel{(b)}{=} \frac{1}{n} \frac{1}{\lambda'} \\ &= \frac{1}{n} \frac{1}{\lambda/n} = \frac{1}{\lambda} \stackrel{(c)}{=} \mathcal{I}_X(\lambda), \end{aligned}$$

where (a) follows from the reparameterization rule for FI [25, (13.21)]; and (b) and (c) from the FI of Poisson parameter  $\theta$  being  $1/\theta$ . For another example, suppose  $X_1, X_2, \dots, X_n$  are i.i.d. Bernoulli random variables with parameter  $p$ . Then  $X = \sum_{i=1}^n X_i$  is a binomial( $n, p$ ) random variable, and well-known FI

expressions give

$$\mathcal{I}_{X_1, X_2, \dots, X_n}(p) = n \mathcal{I}_{X_1}(p) = \frac{n}{p(1-p)} = \mathcal{I}_X(p). \quad (29)$$

It is the compound nature of FIB microscopy measurements creates the potential for improvement from TR sensing.

## Appendix A. Neyman Type A distribution of the number of secondary electrons

We wish to derive the PMF of  $Y$  in (1), where  $M \sim \text{Poisson}(\lambda)$  and  $X_i \sim \text{Poisson}(\eta)$  for each  $i$ . Since the sum of a deterministic number of Poisson random variables is a Poisson random variable, given  $M = m$ ,  $Y$  is a Poisson random variable with mean  $m\eta$ . The PMF of  $Y$  can now be derived by marginalizing the joint PMF of  $Y$  and  $M$  over  $M$ :

$$\begin{aligned} P_Y(y) &= \sum_{m=0}^{\infty} P_{Y,M}(y, m) \stackrel{(a)}{=} \sum_{m=0}^{\infty} P_{Y|M}(y|m) P_M(m) \\ &\stackrel{(b)}{=} \sum_{m=0}^{\infty} \frac{e^{-m\eta} (m\eta)^y}{y!} \frac{e^{-\lambda} \lambda^m}{m!} = \frac{e^{-\lambda} \eta^y}{y!} \sum_{m=0}^{\infty} \frac{(\lambda e^{-\eta})^m m^y}{m!}, \end{aligned}$$

where (a) follows from the multiplication rule; and (b) from substituting Poisson PMFs. This verifies (2). The mean in (3) and variance in (4) follow from the laws of total expectation and of total variance, each applied with conditioning on  $M$ .

## Appendix B. Derivation of Fisher information under Neyman Type A model

For derivation of (12), let us first write  $\log P_Y(y; \eta, \lambda)$  using (2):

$$\log P_Y(y; \eta, \lambda) = -\lambda + y \log \eta - \log y! + \log \left( \sum_{m=0}^{\infty} \frac{(\lambda e^{-\eta})^m m^y}{m!} \right).$$

Taking the derivative with respect to  $\eta$ , we find

$$\begin{aligned} \frac{\partial \log P_Y(y; \eta, \lambda)}{\partial \eta} &= \frac{y}{\eta} - \frac{\sum_{m=0}^{\infty} \frac{m(\lambda e^{-\eta})^m m^y}{m!}}{\sum_{m=0}^{\infty} \frac{(\lambda e^{-\eta})^m m^y}{m!}} \\ &= \frac{y}{\eta} - \frac{\sum_{m=0}^{\infty} \frac{(\lambda e^{-\eta})^m m^{y+1}}{m!}}{\sum_{m=0}^{\infty} \frac{(\lambda e^{-\eta})^m m^y}{m!}} \\ &\stackrel{(a)}{=} \frac{y}{\eta} - \frac{P_Y(y+1; \eta, \lambda) \left| \frac{e^{-\lambda} \eta^{y+1}}{(y+1)!} \right|}{P_Y(y; \eta, \lambda) \left| \frac{e^{-\lambda} \eta^y}{y!} \right|} \\ &= \frac{y}{\eta} - \frac{P_Y(y+1; \eta, \lambda)}{P_Y(y; \eta, \lambda)} \frac{y+1}{\eta}, \end{aligned}$$

where (a) follows from (2). Then the Fisher information is the second moment of the above expression, which verifies (12).

## Appendix C. Normalized Fisher information limits under Neyman Type A model

### Appendix C.1. Low-dose limit

To evaluate  $\lim_{\lambda \rightarrow 0} \mathcal{I}_Y(\eta; \lambda)/\lambda$ , we first find  $\lambda \rightarrow 0$  limits of expressions that appear in (12), including both the PMF in (2) and the probability ratio  $P_Y(y+1; \eta, \lambda)/P_Y(y; \eta, \lambda)$ .

For  $y = 0$ ,

$$P_Y(0; \eta, \lambda) = \frac{e^{-\lambda} \eta^0}{0!} \sum_{m=0}^{\infty} \frac{(\lambda e^{-\eta})^m m^0}{m!} \\ \stackrel{(a)}{=} e^{-\lambda} \sum_{m=0}^{\infty} \frac{(\lambda e^{-\eta})^m}{m!} \stackrel{(b)}{=} e^{-\lambda} \exp(\lambda e^{-\eta}), \quad (\text{C.1})$$

where (a) follows from  $m^0 = 1$ ; and (b) from identifying the series expansion of the exponential function. Similarly, for  $y = 1$ ,

$$P_Y(1; \eta, \lambda) = \frac{e^{-\lambda} \eta^1}{1!} \sum_{m=0}^{\infty} \frac{(\lambda e^{-\eta})^m m^1}{m!} \\ = (e^{-\lambda} \eta) (\lambda e^{-\eta}) \exp(\lambda e^{-\eta}), \quad (\text{C.2})$$

and for  $y = 2$ ,

$$P_Y(2; \eta, \lambda) = \frac{e^{-\lambda} \eta^2}{2!} \sum_{m=0}^{\infty} \frac{(\lambda e^{-\eta})^m m^2}{m!} \\ = \frac{e^{-\lambda} \eta^2}{2} (\lambda e^{-\eta}) (1 + \lambda e^{-\eta}) \exp(\lambda e^{-\eta}). \quad (\text{C.3})$$

For general  $y > 0$ ,

$$P_Y(y; \eta, \lambda) = \frac{e^{-\lambda} \eta^y}{y!} \sum_{m=0}^{\infty} \frac{(\lambda e^{-\eta})^m m^y}{m!} \\ = \frac{e^{-\lambda} \eta^y}{y!} (\lambda e^{-\eta}) \text{poly}_{y-1}(\lambda e^{-\eta}) \exp(\lambda e^{-\eta}), \quad (\text{C.4})$$

where  $\text{poly}_y(\lambda e^{-\eta})$  is a degree- $y$  polynomial in  $\lambda e^{-\eta}$  with unit constant term. This allows us to conclude, for any  $y > 0$ ,

$$\lim_{\lambda \rightarrow 0} \frac{P_Y(y; \eta, \lambda)}{\lambda} = \frac{\eta^y}{y!} e^{-\eta}. \quad (\text{C.5})$$

From (C.1) and (C.2), we obtain, for  $y = 0$ ,

$$\frac{P_Y(y+1; \eta, \lambda)}{P_Y(y; \eta, \lambda)} = \frac{P_Y(1; \eta, \lambda)}{P_Y(0; \eta, \lambda)} = \eta \lambda e^{-\eta}. \quad (\text{C.6})$$

From (C.2) and (C.3), we obtain, for  $y = 1$ ,

$$\frac{P_Y(y+1; \eta, \lambda)}{P_Y(y; \eta, \lambda)} = \frac{P_Y(2; \eta, \lambda)}{P_Y(1; \eta, \lambda)} = \frac{1}{2} \eta (1 + \lambda e^{-\eta}). \quad (\text{C.7})$$

For general  $y > 0$ , it follows from (C.5) that

$$\lim_{\lambda \rightarrow 0} \frac{P_Y(y+1; \eta, \lambda)}{P_Y(y; \eta, \lambda)} = \frac{\eta}{y+1}. \quad (\text{C.8})$$

Now to evaluate  $\lim_{\lambda \rightarrow 0} \mathcal{I}_Y(\eta; \lambda)/\lambda$ , we can pass the limit through to each term in (12). The first term is

$$\lim_{\lambda \rightarrow 0} \left( \frac{0}{\eta} - \frac{P_Y(1; \eta, \lambda)}{P_Y(0; \eta, \lambda)} \frac{1}{\eta} \right)^2 \frac{P_Y(0; \eta, \lambda)}{\lambda} \\ \stackrel{(a)}{=} \lim_{\lambda \rightarrow 0} \left( \frac{0}{\eta} - \eta \lambda e^{-\eta} \frac{1}{\eta} \right)^2 \frac{e^{-\lambda} \exp(\lambda e^{-\eta})}{\lambda} \\ = 0, \quad (\text{C.9})$$

where (a) follows from (C.1) and (C.6). By substituting (C.5) and (C.8) in (12), the remaining terms give

$$\lim_{\lambda \rightarrow 0} \frac{\mathcal{I}_Y(\eta; \lambda)}{\lambda} = \sum_{y=1}^{\infty} \left( \frac{y}{\eta} - \frac{\eta}{y+1} \frac{y+1}{\eta} \right)^2 \frac{\eta^y}{y!} e^{-\eta} \\ = \sum_{y=1}^{\infty} \left( \frac{y}{\eta} - 1 \right)^2 \frac{\eta^y}{y!} e^{-\eta} \\ = \left( \frac{e^{\eta}}{\eta} - 1 \right) e^{-\eta} = \frac{1}{\eta} - e^{-\eta}.$$

This proves (13), as desired.

### Appendix C.2. High-dose limit

Let us first compute the Fisher information for the parameter  $\eta$  when a Gaussian random variable has mean  $\eta$  and variance  $f(\eta)$  for some twice-differentiable function  $f$ . Let  $S \sim \mathcal{N}(\eta, f(\eta))$ . Then the log-likelihood of  $S$  is

$$\log f_S(s; \eta) = -\frac{1}{2} \log(2\pi) - \frac{1}{2} \log f(\eta) - \frac{(s-\eta)^2}{2f(\eta)}. \quad (\text{C.10})$$

The derivative of  $\log f_S(s; \eta)$  with respect to  $\eta$  is

$$\frac{\partial \log f_S(s; \eta)}{\partial \eta} = -\frac{f'(\eta)}{2f(\eta)} - \frac{2(\eta-s)f(\eta) - (\eta-s)^2 f'(\eta)}{2f(\eta)^2}.$$

The second derivative is then

$$\frac{\partial^2 \log f_S(s; \eta)}{\partial \eta^2} = -\frac{f''(\eta)f(\eta) - f'(\eta)^2}{2f(\eta)^2} - \frac{1}{f(\eta)} + \frac{2f'(\eta)}{f(\eta)^2}(\eta-s) \\ - \frac{2[f'(\eta)]^2 - f''(\eta)f(\eta)}{2f(\eta)^3}(\eta-s)^2.$$

The Fisher information for the estimation of  $\eta$  is

$$\mathcal{I}_S(\eta) = \mathbb{E} \left[ -\frac{\partial^2 \log f_S(S; \eta)}{\partial \eta^2} ; \eta \right] \\ = \frac{f''(\eta)f(\eta) - f'(\eta)^2}{2f(\eta)^2} + \frac{1}{f(\eta)} - \frac{2f'(\eta)}{f(\eta)^2} \mathbb{E}[\eta - S] \\ + \frac{2[f'(\eta)]^2 - f''(\eta)f(\eta)}{2f(\eta)^3} \mathbb{E}[(\eta - S)^2] \\ \stackrel{(a)}{=} \frac{f''(\eta)f(\eta) - f'(\eta)^2}{2f(\eta)^2} + \frac{1}{f(\eta)} - \frac{2f'(\eta)}{f(\eta)^2} \cdot 0 \\ + \frac{2[f'(\eta)]^2 - f''(\eta)f(\eta)}{2f(\eta)^3} \cdot f(\eta) \\ = \frac{1}{f(\eta)} + \frac{[f'(\eta)]^2}{2f(\eta)^2}, \quad (\text{C.11})$$

where (a) follows from substituting  $E[\eta - S] = 0$  and  $E[(\eta - S)^2] = \text{var}(S) = f(\eta)$ . (Note that this simplifies to the familiar reciprocal of the variance when  $f(\eta)$  is a constant.)

At high dose,  $Y/\lambda$  is well-approximated as a  $\mathcal{N}(\eta, \eta(\eta+1)/\lambda)$  random variable [18, Sect. IV]. Thus, define  $f(\eta) = \eta(\eta+1)/\lambda$  so that  $Y/\lambda$  is approximated well by  $S$ . Substituting  $f'(\eta) = (2\eta+1)/\lambda$  into (C.11) gives

$$\mathcal{I}_S(\eta) = \frac{\lambda}{\eta(\eta+1)} + \frac{(2\eta+1)^2}{2\eta^2(\eta+1)^2}. \quad (\text{C.12})$$

Since  $Y \approx \lambda S$ ,

$$\lim_{\lambda \rightarrow \infty} \frac{\mathcal{I}_Y(\eta; \lambda)}{\lambda} = \lim_{\lambda \rightarrow \infty} \left[ \frac{1}{\eta(\eta+1)} + \frac{(2\eta+1)^2}{2\lambda\eta^2(\eta+1)^2} \right] = \frac{1}{\eta(\eta+1)},$$

as desired.

## Declarations of interest

The authors declare no competing financial interests.

## Author contributions

KKB and VKG conceived of time-resolved measurement in FIB microscopy. MP, JMB, and VKG derived the mathematical results. MP wrote software for image formation and completed all numerical experiments. MP, JMB, and VKG wrote the manuscript. All authors edited the manuscript.

## Acknowledgments

The authors thank John Notte and Deying Xia of Carl Zeiss Microscopy LLC for enlightening discussions and experimental data and images.

Funding: This material is based upon work supported in part by the US National Science Foundation under Grant No. 1422034 and Grant No. 1815896.

## References

- [1] D. McMullan, Scanning electron microscopy 1928–1965, *Scanning* 17 (3) (1995) 175–185.
- [2] M. Minsky, Memoir on inventing the confocal scanning microscope, *Scanning* 10 (4) (1988) 128–138.
- [3] W. Denk, J. H. Strickler, W. W. Webb, Two-photon laser scanning fluorescence microscopy, *Science* 248 (4951) (1990) 73–76.
- [4] B. W. Ward, J. A. Notte, N. P. Economou, Helium ion microscope: A new tool for nanoscale microscopy and metrology, *J. Vac. Sci. & Technol. B* 24 (6) (2006) 2871–2874.
- [5] M. Peng, J. Murray-Bruce, K. K. Berggren, V. K. Goyal, Source shot noise mitigation in scanned beam microscopy, in: *Proc. 62nd Int. Conf. Electron, Ion, Photon Beam Technologies and Nanofabrication*, Rio Mar, PR, 2018.
- [6] J. C. H. Spence, Diffractive (lensless) imaging, in: *Science of Microscopy*, Springer, 2007, pp. 1196–1227.
- [7] N. P. Economou, J. A. Notte, W. B. Thompson, The history and development of the helium ion microscope, *Scanning* 34 (2) (2012) 83–89.
- [8] M. S. Joens, C. Huynh, J. M. Kasuboski, D. Ferranti, Y. J. Sigal, F. Zeitvogel, M. Obst, C. J. Burkhardt, K. P. Curran, S. H. Chalasani, et al., Helium ion microscopy (HIM) for the imaging of biological samples at sub-nanometer resolution, *Sci. Rep.* 3 (2013) 3514.
- [9] R. Ramachandra, B. Griffin, D. Joy, A model of secondary electron imaging in the helium ion scanning microscope, *Ultramicroscopy* 109 (6) (2009) 748–757.
- [10] M. Schürmann, N. Frese, A. Beyer, P. Heimann, D. Widera, V. Mönkemöller, T. Huser, B. Kaltschmidt, C. Kaltschmidt, A. Götzhäuser, Helium ion microscopy visualizes lipid nanodomains in mammalian cells, *Small* 11 (43) (2015) 5781–5789.
- [11] V. Castaldo, C. W. Hagen, P. Kruit, Simulation of ion imaging: Sputtering, contrast, noise, *Ultramicroscopy* 111 (8) (2011) 982–994.
- [12] V. Castaldo, C. W. Hagen, P. Kruit, E. Van Veldhoven, D. Maas, On the influence of the sputtering in determining the resolution of a scanning ion microscope, *J. Vac. Sci. & Technol. B* 27 (6) (2009) 3196–3202.
- [13] J. Orloff, L. W. Swanson, M. Utlaut, Fundamental limits to imaging resolution for focused ion beams, *J. Vac. Sci. & Technol. B* 14 (6) (1996) 3759–3763.
- [14] D. Fox, Y. B. Zhou, A. O'Neill, S. Kumar, J. J. Wang, J. N. Coleman, G. S. Duesberg, J. F. Donegan, H. Z. Zhang, Helium ion microscopy of graphene: Beam damage, image quality and edge contrast, *Nanotechnology* 24 (33) (2013) 335702.
- [15] R. Livengood, S. Tan, Y. Greenzweig, J. Notte, S. McVey, Subsurface damage from helium ions as a function of dose, beam energy, and dose rate, *J. Vac. Sci. & Technol. B* 27 (6) (2009) 3244–3249.
- [16] J. Cazaux, Calculated influence of work function on SE escape probability and secondary electron emission yield, *Applied Surface Science* 257 (3) (2010) 1002–1009.
- [17] J. Neyman, On a new class of “contagious” distributions, applicable in entomology and bacteriology, *Ann. Math. Statist.* 10 (1) (1939) 35–57.
- [18] M. C. Teich, Role of the doubly stochastic Neyman type-A and Thomas counting distributions in photon detection, *Appl. Optics* 20 (14) (1981) 2457–2467.
- [19] J. W. Ward, R. L. Kubena, R. J. Joyce, An ion counting apparatus for studying the statistics of ion emission from liquid metal ion sources, *J. Vac. Sci. & Technol. B* 9 (6) (1991) 3090–3094.
- [20] S. M. Kay, *Fundamentals of Statistical Signal Processing: Estimation Theory*, Prentice-Hall, Inc., Upper Saddle River, NJ, USA, 1993.
- [21] J. A. Notte, Imaging with helium ions – A new detector regime with new challenges and new opportunities, presented at the American Vacuum Society 60th Int. Symp. Exhibit., October 31 (no proceedings) (2013).
- [22] J. Notte, R. Hill, S. McVey, L. Farkas, R. Percival, B. Ward, An introduction to helium ion microscopy, *Microscopy and Microanalysis* 12 (S02) (2006) 126–127.
- [23] J. Notte, B. Ward, N. Economou, R. Hill, R. Percival, L. Farkas, S. McVey, An introduction to the helium ion microscope, in: *AIP Conference Proceedings*, Vol. 931, AIP, 2007, pp. 489–496.
- [24] T. Hakamata, et al., *Photomultiplier Tubes: Basics and Applications*, 3rd Edition, Hamamatsu Photonics K. K., 2007.
- [25] E. L. Lehman, G. Casella, *Theory of Point Estimation*, 2nd Edition, Springer, New York, NY, USA, 1998.